RSC Advances

ROYAL SOCIETY OF CHEMISTRY

www.rsc.org/advances

A novel apatite-based warm white emitting phosphor $Ba_3GdK(PO_4)_3F:Tb^{3+},Eu^{3+}$ with efficient energy transfer for w-LEDs

Chao Zeng,[†] Yingmo Hu[*,†], Zhiguo Xia,[†] Hongwei Huang[*,†]

†Beijing Key Laboratory of Materials Utilization of Nonmetallic Minerals and Solid

Wastes, National Laboratory of Mineral Materials, School of Materials Science and

Technology, China University of Geosciences, Beijing 100083, China

E-mail: huyingmo@cugb.edu.cn; hhw@cugb.edu.cn.

$Ba_3GdK(PO_4)_3F:Tb^{3+},Eu^{3+}$ phosphor with fluoro-apatite-structure has been fabricated

by conventional high-temperature solid-state reaction. The crystal structure,

component element and microstructure of the phosphor have been systematically

investigated by X-ray diffraction refinement, X-ray photoelectron spectroscopy (XPS),

scanning electron microscope (SEM), transmission electron microscopy (TEM) and

high-resolution TEM (HRTEM), respectively. $Ba_3GdK(PO_4)_3F:Tb^{3+}$ phosphor shows

blue-greenish emission peak at 547 nm under excitation of 276 nm, while

$Ba_3GdK(PO_4)_3F:Eu^{3+}$ displays the red emission peak near 620 nm with excitation at

396nm. Efficient energy transfer from Tb^{3+} to Eu^{3+} ions takes place in the

$Ba_3GdK(PO_4)_3F$ host, and the energy transfer critical distance between Tb^{3+} and Eu^{3+}

along with resonant energy-transfer mechanism are determined. By tuning Tb^{3+}/Eu^{3+}

ratio, the emission hue can be modulated from blue-green (0.238, 0.311) to white

(0.341, 0.318) and eventually to orange (0.521, 0.335). Moreover, the thermal

quenching property of as-prepared samples was studied in detail, which discloses the

high thermal stability.

KEYWORDS: *fluoro-apatite-structure, white-light-emitting phosphor, energy transfer, high thermal stabilities*

1、Introduction

White light-emitting diodes (*w*-LEDs) has been verified to possess lots of advantages, such as high luminescence efficiency, long lifetime, low power consumption, high brightness and environmental friendliness, which can been applied in displays and lighting sources [1-4]. Currently, the most frequent way to fabricate *w*-LEDs is combining a blue-emitting LED chip with a single yellow-emitting phosphor $(Y_3Al_5O_{12}:Ce^{3+})$ [5-7]. However, this type of white light have some limitations, for example, low color rendering index (Ra < 80) and high correlated color temperature (Tc > 4500 K) due to the lack of red or orange emission, color change according to the input power, and poor thermal stability [8-10]. Accordingly, an alternative approach to obtaining white light is combining near-UV (380-420nm) LED with tri-color (blue, green, red) phosphors. It can offer suitable correlated color temperature and high color rendering index of light [11-12]. Whereas, the manufacture cost of three converter (RGB) systems is high. Moreover, the blue emission efficiency is low because of the strong absorption of the blue light by the red and green phosphors [13]. To overcome the above-mentioned drawbacks, single-component white phosphors with high efficiency and excellent color rendering index are highly desirable.

The Eu^{3+} ion is a renowned red emission emitting activator according to $^5D_0$-^7F_J transition. Particularly, the emission line of Eu^{3+} ions is slight host-dependence, which

is beneficial to lumen equivalency and color rendering[14]. On the other hand, Tb^{3+}

ions exhibit the emission lines in the blue and green regions, corresponding to $^5D_3$-^7F_J

and $^5D_4$-^7F_J transition, respectively. There are many papers reporting that effective

energy transfer from Tb^{3+} to Eu^{3+} can take place in several hosts. For example,

$Ba_3La(PO_4)_3$:Tb^{3+}/Eu^{3+}[15]; $Ca_3Bi(PO_4)_3$:Eu^{3+}/Tb^{3+}/Tm^{3+}[16]; $NaGd(PO_3)_4$:Tb^{3+}/Eu^{3+}[17];

$NaCaPO_4$:Tb^{3+}/Eu^{3+}[18]; $YCa_4O(BO_3)_3$:Tb^{3+}/Eu^{3+}[19]; $KCaY(PO_4)_2$:Tb^{3+}/Eu^{3+}[20], and

so on. Thus, it is available to improve the Eu^{3+} ions emission intensity by co-doping

Tb^{3+} ions.

Recently, researches on apatite-type phosphors are very active because of their

excellent chemical and thermal stability. Among them, phosphor matrix with apatite

type alkaline-earth halo-phosphates has a general chemical formula as $A_{10}[RO_4]_6Z_2$,

where A often represents a univalent to trivalent cation such as Na^+, K^+, Rb^+, Ca^{2+},

Mg^{2+}, Ba^{2+}, Fe^{2+}, Sr^{2+}, Mn^{2+}, Pb^{2+}, Gd^{3+}, Lu^{3+},Y^{3+} and so on; R is P^{5+}, Ge^{4+}, Si^{4+}, V^{5+},

etc; while Z can be F^-, Br^-, Cl^-, OH^- and O^{2-}. In addition, the fluorine atoms keep the

largest electronegative and show strongest attractive electron ability, so apatite

structure phosphors with fluorine atoms always have fluorescence property with high

intensity.[21] Since Zhang etc. firstly synthesized Ce^{3+}, Mn^{2+}-doped $Ca_5(PO_4)_3F$ via

hydrothermal method and systematically investigated its luminescence properties in

2010,a series of rare-earth doped phosphors with apatite structure, for example,

$Ca_4Y_6(SiO_4)_6O$: Ce^{3+}, Tb^{3+}[22], $Ca_9Mg(PO_4)_6F_2$: Eu^{2+}, Mn^{2+}[23], $Ba_3LaNa(PO_4)_3F$: Eu^{2+},

Tb^{3+}[21], $Sr_5(PO_4)_3Cl$:Ce^{3+}, Eu^{2+}[24], $Ca_6Y_2Na_2(PO_4)_6F_2$:Eu^{2+},Mn^{2+}[25]; $Sr_3NaLa(PO_4)_3F$:

Eu^{2+},Mn^{2+}[26] have been well studied. However, there have no reports about

$Ba_3GdK(PO_4)_3F$: Tb^{3+}, Eu^{3+} phosphors. In this work, we report the synthesis, structure and photoluminescence of Tb^{3+}/Eu^{3+} activated $Ba_3GdK(PO_4)_3F$, which can act as a single-component warm-white-emitting conversion phosphor for UV-based white LEDs. Via the Eu^{3+} concentration regulation, the emitting color of this new phosphor can modulated from blue-greenish through white, and eventually to orange. The corresponding critical distances (R_C) of Tb^{3+}/Eu^{3+}were calculated and the energy transfer properties from Tb^{3+} to Eu^{3+} were investigated systematically. In addition, the temperature-dependent emission spectra have been investigated and the phosphors exhibit outstanding thermal stability.

2. Experimental section

2.1. Materials and Synthesis.

All the powder samples $Ba_3GdK(PO_4)_3F$ and $Ba_3Gd_{1-m-n}K(PO_4)_3F:mTb^{3+},nEu^{3+}$ were prepared by a traditional solid-state reaction utilizing stoichiometric amounts of $BaCO_3$, Gd_2O_3, K_2CO_3, $(NH_4)H_2PO_4$, NH_4HF_2, Tb_4O_7 and Eu_2O_3. After grinding thoroughly, the mixture was put in an aluminum crucible and fired at 1080℃ for 3h. After cooling to room temperature, the samples were ground again into powder for measurement.

2.2. Characterization.

The crystalline phases of synthesized products were examined by powder X-ray diffraction (XRD, XD-3, PGENERAL, China) in the 2θ range from 10° to 70°, with graphite monochromatized Cu Kα radiation (λ = 0.15406 nm) operating at 40 kV and 30 mA. The step scanning rate (2θ ranging from 5° to 100°) used for Rietveld analysis

was 3 s/step with a step size of 0.04. Powder diffraction data were obtained by the Rietveld method using the computer software General Structure Analysis System (GSAS) program. The X-ray photoelectron spectroscopy (XPS) was obtained on a ESCALAB 250xi (ThermoFsher, England) electron spectrometer. Scanning electron microscope (SEM) and transmission electron microscopy (TEM) were performed by JSM-IT300 (Japan), and JEM-2100, respectively. The photoluminescence emission (PL) and photoluminescence excitation (PLE) spectra of the as-prepared powders were recorded using a Hitachi F-4600 fluorescence spectrophotometer PL system equipped with a xenon lamp (400V, 150W) as an excitation source, and a 400 nm cutoff filter that was used to eliminate the second-order emission of source radiation in the measurement. Diffuse reflection spectra were characterized on a Shimadzu UV-3600 UV-vis-NIR spectrophotometer attached with an integral sphere. The luminescence decay curve was obtained from a spectrofluorometer (HORIBA, JOBIN YVON FL3-21) with a 370 nm pulse laser radiation (nano-LED) as the excitation source, and the pulse width of the laser was 12 ns. All the above-mentioned measurements were performed at room temperature. The temperature-dependence luminescence properties were identified on the same spectrophotometer, combined with a self-made heating attachment and a computer-controlled electric furnace.

3. Results and discussion

Fig. 1 shows the powder XRD pattern of $Ba_3GdK(PO_4)_3F$ sample by using the computer software General Structure Analysis System (GSAS) program[27]. In this study, we have refined the $Ba_3GdK(PO_4)_3F$ sample with the structural model

$Ba_3LaNa(PO_4)_3F$[28] for their similar apatite crystal structures, and the results show that the data and the structural model are in good agreement. Fractional atomic coordinates, occupancies and isotropic thermal parameters of this sample are presented in **Table 1**, K^+ and Gd^{3+} are designed to occupy in the sites of Na^+ and La^{3+}, respectively, because of the similar ion radius and the equal charge number[29]. $Ba_3GdK(PO_4)_3F$ crystallizes in the hexagonal crystal system with space group *P-6*. Its unit cell parameters *a*=9.855(36)Å, *c*=7.484(02)Å, *V*=629.522Å^3 differ from that of $Ba_3LaNa(PO_4)_3F$ (*a*=9.939(24) Å, *c*= 7.441(95) Å, *V* =636.670Å^3), which is resulted from the substitution of Na^+ by K^+ and La^{3+} by Gd^{3+} according to Vegard's rule[30]. **Fig. 2 a** shows the schematic illustration of the crystal structure of $Ba_3GdK(PO_4)_3F$ viewed from the *c* axis. In this crystal structure, there exist four cationic sites Ba2/K1, Ba1/Gd1, Gd2/K2 and Ba3/K3. There are two cationic sites in apatite host $Ba_3GdK(PO_4)_3F$ coordinated by seven(M1) and nine(M2) O^{2-}/F^- ions, where Ba1/Gd1 ions site in M1 coordinated by 5O and 2F, and Gd2/K2 and Ba3/K3 ions coordinated by 9O and Ba2/K1 coordinated by 7O and 2F occupy in M2. The coordination environment around the four cationic sites Ba2/K1, Ba1/Gd1, Gd2/K2 and Ba3/K3 are given in **Fig. 2 b.** In addition, **Fig. 3** displays the XRD patterns of $Ba_3Gd_{0.95-n}K(PO_4)_3F:0.05Tb^{3+},nEu^{3+}(0 \leq n \leq 0.40)$ samples and the standard cards of JCPDS 71-1317 ($Ba_3LaNa(PO_4)_3F$). It can be found that all the diffraction peaks of the $Ba_3Gd_{0.95-n}K(PO_4)_3F:0.05Tb^{3+},nEu^{3+}$ are well-indexed to the standard data. This result suggests that the as-prepared samples are single phase and the Tb^{3+}, Eu^{3+} ions have been incorporated into the host lattice without causing any significant change.

With a view to the ionic radius and valence state, it is believed that the Tb^{3+}/Eu^{3+} would occupy the Gd^{3+} sites.

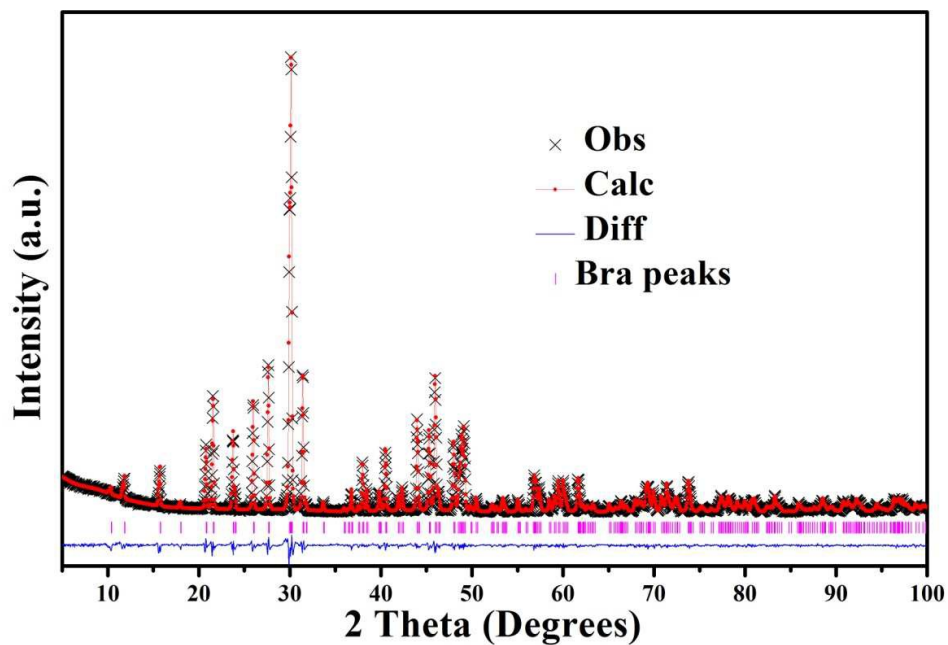**Fig. 1.** Powder XRD patterns for Rietveld structure analysis of the selected $Ba_3GdK(PO_4)_3F$ phosphor based on the $Ba_3LaNa(PO_4)_3F$-ICSD-10030 phase model.

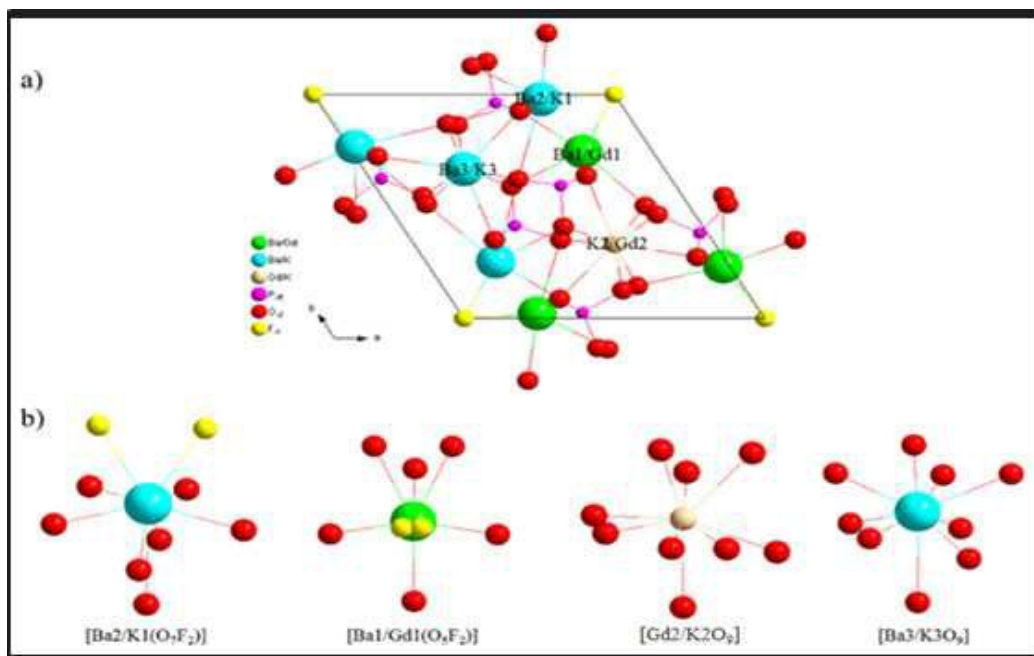**Fig. 2.** Schematic illustration of the crystal structure of $Ba_3GdK(PO_4)_3F$ viewed from the c axis, and the coordination environment around Ba2/K1, Ba1/Gd1, Gd2/K2 and Ba3/K3.

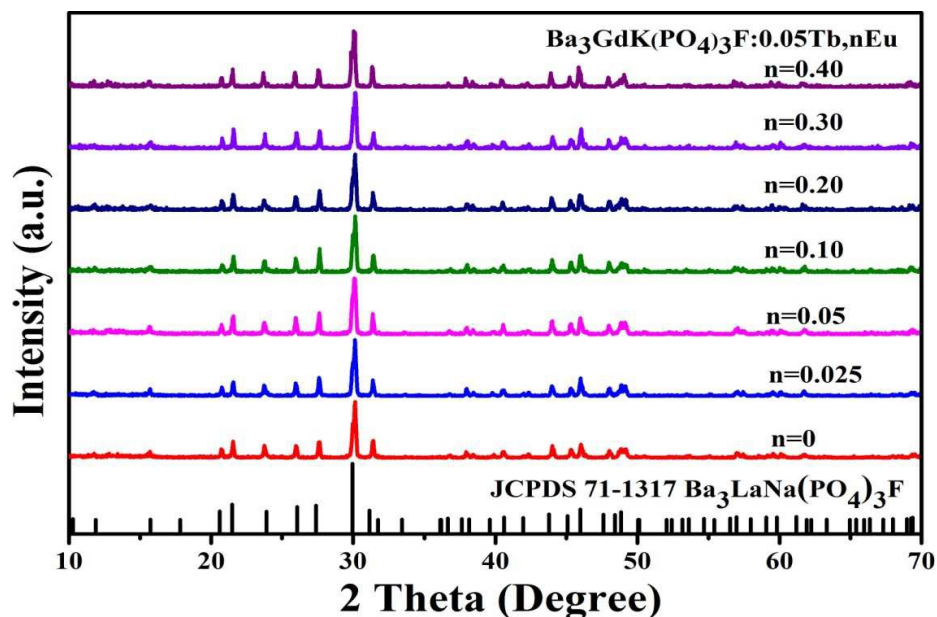**Fig. 3**. XRD patterns of $Ba_3GdK(PO_4)_3F$: $0.05Tb^{3+}$,nEu^{3+} ($0 \leq n \leq 0.40$) samples and the standard data for $Ba_3LaNa(PO_4)_3F$ (JCPDS No.71-1317).

Table 1. Fractional atomic coordinates, occupancies and isotropic thermal parameters of $Ba_3GdK(PO_4)_3F$ obtained from the GSAS Rietveld Refinement using X-ray powder diffraction data at room temperature.

Atom	x	y	z	Occupancy	Uiso/Å^2	Mult
Ba1	0.2484(36)	0.0247(91)	1/2	2/3	0.009(36)	3
Gd1	0.2484(36)	0.0247(91)	1/2	1/3	0.009(36)	3
Ba2	0.0170(84)	0.7583(36)	0.0	0.904	0.015(16)	3
K1	0.0170(84)	0.7583(36)	0.0	0.096	0.015(16)	3
Gd2	2/3	1/3	0.2480(30)	1/2	0.029(44)	2
K2	2/3	1/3	0.2480(30)	1/2	0.029(44)	2
Ba3	1/3	2/3	0.2310(28)	0.645	0.002(06)	2
K3	1/3	2/3	0.2310(28)	0.355	0.002(06)	2
P1	0.4093(09)	0.4496(51)	1/2	1.0	0.244 (52)	3
P2	0.6280(99)	0.6043(67)	0.0	1.0	0.014(60)	3
O1	0.4970(00)	0.3510(00)	1/2	1.0	0.116(00)	3
O2	0.4530(00)	0.5900(00)	1/2	1.0	0.012(99)	3
O3	0.2770(00)	0.3510(00)	0.3500(00)	1.0	0.012(36)	6
O4	0.4900(00)	0.6210(00)	0.0	1.0	0.035(97)	3

O5	0.53600(00)	0.4100(00)	0.0	1.0	0.080(49)	3
O6	0.72600(00)	0.6380(00)	0.1790(00)	1.0	0.201(83)	6
F1	0.0	0.0	0.5788(36)	1/2	0.015(17)	2
F2	0.0	0.0	0.3128(23)	1/2	0.015(17)	2

space group: *P -6* - hexagonal; *a* = *b* = 9.855(36) Å, *c* = 7.484(02) Å, *V* = 629.522Å³;

α=β= 90º, γ=120º; 2θ-interval = 5-100º; *R_{wp}(%)* = 4.06, *Rp(%)*=2.47, *x^2*=2.32

To determine the element composition and the chemical states of europium, X-ray photoelectron spectroscopy (XPS) analysis was carried out on $Ba_3Gd_{0.925}K(PO_4)_3F:0.05Tb^{3+},0.025Eu^{3+}$, as shown in **Fig. 4**. From **Fig. 4**, a typical survey XPS spectrum of $Ba_3Gd_{0.925}K(PO_4)_3F: 0.05Tb^{3+}, 0.025Eu^{3+}$ contains the main peaks corresponding to Ba $3d_3$, Ba $3d_5$, O 1s, Tb 3d, P 2p, Gd $4d_5$, K $2p_3$, F 1s, C 1s, and Eu 3d. The C peak is because of the adventitious hydrocarbon of the XPS instrument. The binding energies around 795.2, 780.0, 292.9, 142.4, 530.6, 683.5, 1240 and 1136 eV corresponds well to the Ba^{2+}, K^+, Gd^{3+}, O^{2-}, F^-, Tb^{3+}, and Eu^{3+} ions respectively.[31-32] In particular, the characteristic peak of Eu^{2+} ions has not been found. Combined with the XRD analysis, it can be confirmed that the $Ba_3Gd_{0.925}K(PO_4)_3F: 0.05Tb^{3+},0.025Eu^{3+}$ phosphor is successfully developed.
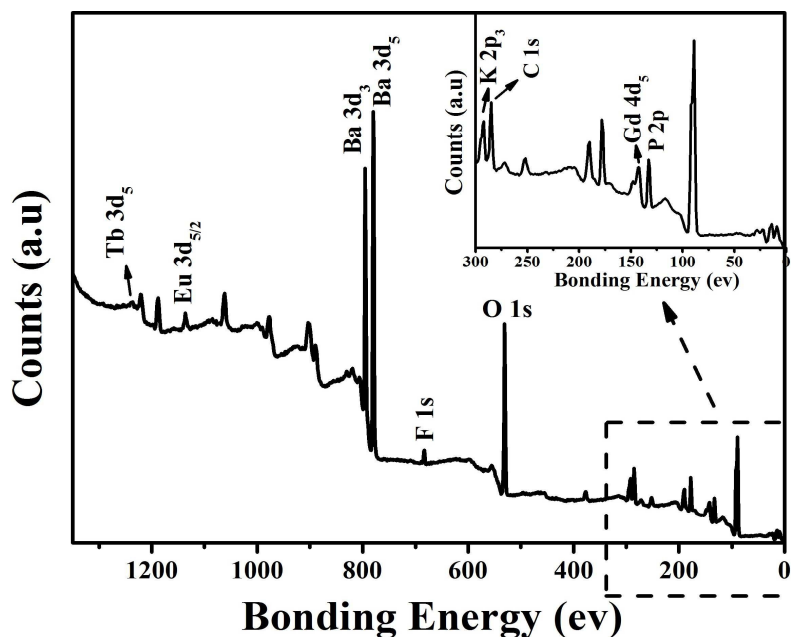
Fig. 4 High-resolution XPS survey spectrum of $Ba_3GdK(PO_4)_3F:0.05Tb^{3+},0.025Eu^{3+}$.

For the purpose of investigating the morphology and structure of the final products, scanning electron microscope(SEM) and transmission electron microscopy(TEM) were performed on the $Ba_3Gd_{0.925}K(PO_4)_3F:0.05Tb^{3+},0.025Eu^{3+}$ phosphor. As shown in **Fig. 5(a)**, the sample exhibits regularly parallelepiped-like structure with particle size ranging from 2 to 4 μm. This observation suggests that the phosphor is of high crystallinity. **Fig. 5(b)** depicts the TEM image of the $Ba_3Gd_{0.925}K(PO_4)_3F:0.05Tb^{3+},0.025Eu^{3+}$ crystal. The fine structure recorded by HRTEM was analyzed by Digital Micrograph software. The fast Fourier transform (FFT) image, as portrayed in the inset of **Fig. 5(c),** further demonstrates the perfect single-crystalline nature. The distance between the adjacent fringes was determined to be 0.325 nm, corresponding well with the (120) plane of the pure $Ba_3GdK(PO_4)_3F$: $0.05Tb^{3+}$, $0.025Eu^{3+}$ phase.
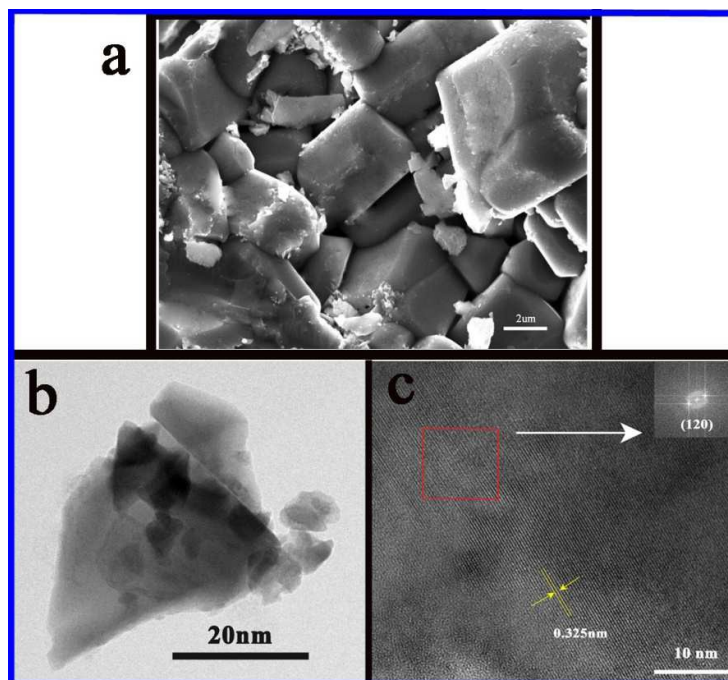
Fig. 5 (a) SEM image, **(b)** TEM image, and **(c)** HRTEM images of $Ba_3GdK(PO_4)_3F:0.05Tb^{3+}$, $0.025Eu^{3+}$. Inserts in parts **c** is the fast Fourier transforms (FFTs) of the relevant HRTEM images.

To investigate the effect of Tb^{3+} doping content on luminescence properties, we synthesize a series of $Ba_3Gd_{1-m}K(PO_4)_3F:mTb^{3+}$ (m = 0.025, 0.05, 0.10, 0.20, 0.30, 0.40) phosphors. **Fig. 6** presents the PL spectra of $Ba_3Gd_{1-m}K(PO_4)_3F:mTb^{3+}$ with different doping contents. It can be observed that the emission spectra of $Ba_3Gd_{1-m}K(PO_4)_3F:mTb^{3+}$ present the $^5D_{3,4} \rightarrow {}^7F_J$ transitions of Tb^{3+} ions. The green emission lines between 490 and 630 nm are ascribed to the $^5D_4-{}^7F_J$ (J = 6, 5, 4, 3) transitions, while the blue emission lines from 380 to 480 nm are attributed to the $^5D_3-{}^7F_J$ transitions. At first, the $^5D_3 \rightarrow {}^7F_J$ transitions is dominant with low doping concentrations (m) in the emission spectra, and the $^5D_4 \rightarrow {}^7F_5$ transition at 546 nm plays an increasingly dominant role with enhancing the doping concentrations. The quenching of the blue emissions of $^5D_3 \rightarrow {}^7F_J$ transitions is due to the cross-relaxation between the $^5D_3-{}^5D_4$ and $^7F_0-{}^7F_6$ of the two adjacent Tb^{3+} ions. In addition, the green

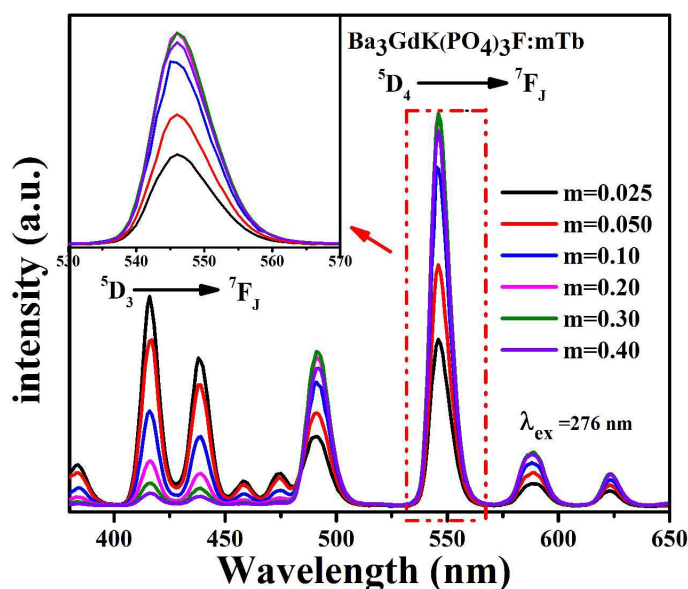emissions of the $^5D_4 \to {}^7F_J$ transitions are quenched via the energy migration between the activators [33].

Fig. 6 PL spectra of $Ba_3GdK(PO_4)_3F:Tb^{3+}$ with various doping concentration of Tb^{3+}.

Fig. 7 shows the photoluminescence spectra of Tb^{3+} and/or Eu^{3+} in the $Ba_3GdK(PO_4)_3F$ host lattice. **Fig. 7(a)** displays the PLE and PL spectra of $Ba_3Gd_{0.95}K(PO_4)_3F:0.05Tb^{3+}$ phosphor. Under the excitation of 276nm, the as-prepared $Ba_3Gd_{0.95}K(PO_4)_3F:0.05Tb^{3+}$ phosphor exhibits two sets of emission bands. The emission peaks at 491, 547, 589, and 623 nm are ascribed to the $^5D_4-{}^7F_J$ (J = 6, 5, 4, 3) transitions, while the emission peaks at 384, 417,438, 458and 474 nm are attributed to the $^5D_3-{}^7F_J$ (J = 6, 5, 4, 3) transitions. The PLE spectrum monitored at emission wavelength of 547nm exhibits a broad band and several weak peaks. The two asymmetric lines from 200 to 240 nm and 270 to 300 nm are due to the Tb^{3+} ions f−f transitions. In addition, this phosphor exhibits a broad absorption band from 200 to 400nm, matching well with UV-LED chip. Meanwhile, the peaks at 312, 342, 353, 371 and 488nm should be assigned to the Tb^{3+} transition of $^7F_6-{}^5H_6$ (305 nm), $^7F_6-{}^5D_0$

(321 nm), $^7F_6$-$^5D_2$ (356 nm), $^7F_6$-$^5G_6$ (371 nm) and $^7F_6$-$^5D_4$ (489 nm), respectively [34-35].

Fig. 7(b) shows that the PL spectra of $Ba_3Gd_{0.975}K(PO_4)_3F:0.025Eu^{3+}$ with excitation wavelength of 396nm containing several sharp peaks. The peaks at 595, 620, 659 and 701nm are due to the transitions from the $^5D_0$ ground state to the $^7F_0$ (561nm), $^7F_1$ (595nm), $^7F_2$ (620 nm), $^7F_3$ (659 nm), and $^7F_4$ (701 nm) excited levels of Eu^{3+} ions, respectively. Monitored by the emission at 620nm, the excitation spectrum of $Ba_3Gd_{0.975}K(PO_4)_3F:0.025Eu^{3+}$ shows a broad band and several weak peaks. The broad band from 200 to 300nm is attributed to the charge transfer band (CTB) between O^{2-} and Eu^{3+} ions. The sharp peaks observed between 300–500nm are assigned to the f-f transitions of Eu^{3+} ions, which correspond to $^7F_0 \rightarrow {}^5H_3$ (313 nm), $^7F_0 \rightarrow {}^5L_9$ (364 nm), $^7F_0 \rightarrow {}^5G_3$ (384nm) and $^7F_0 \rightarrow {}^5L_6$ (396 nm) transitions [36-38]. According to **Fig. 7(a)** and **7(b)**, the significant spectral overlap between the emission band of $Ba_3Gd_{0.95}K(PO_4)_3F:0.05Tb^{3+}$ and the excitation band of $Ba_3Gd_{0.975}K(PO_4)_3F:$ $0.025Eu^{3+}$ can be observed, which indicate that energy transfer from Tb^{3+} to Eu^{3+} in the $Ba_3GdK(PO_4)_3F$ host occurred.

Fig. 7(c) depicts the PL and PLE spectra of $Ba_3Gd_{0.925}K(PO_4)_3F:$ $0.05Tb^{3+},0.025Eu^{3+}$. The PLE spectrum measured by the Eu^{3+} emission at 620nm is the combination of the PLE of Eu^{3+} and Tb^{3+} in $Ba_3GdK(PO_4)_3F$, confirming that the Eu^{3+} ions are essentially excited by the Tb^{3+} ions. This result reveals that an efficient energy transfer from the Tb^{3+} to Eu^{3+} ions takes place. With excitation at 276nm, the emission spectrum of $Ba_3Gd_{0.925}K(PO_4)_3F:$ $0.05Tb^{3+},0.025Eu^{3+}$ exhibits a broad

blue-greenish band and a red emission band. The blue-greenish lines from 400 to 570nm correspond to the f-f transition of Tb^{3+} ions, and the red emission lines from 570 to 730nm are attributed to the f-f transition of Eu^{3+} ions, principally. The emission spectrum nearly covers the entire visible region. Therefore, a warm white light may be obtained by combining the blue-greenish emission of the Tb^{3+} ions with the red emission of the Eu^{3+} ions via the partial energy transfer between the Tb^{3+} and the Eu^{3+} ions.
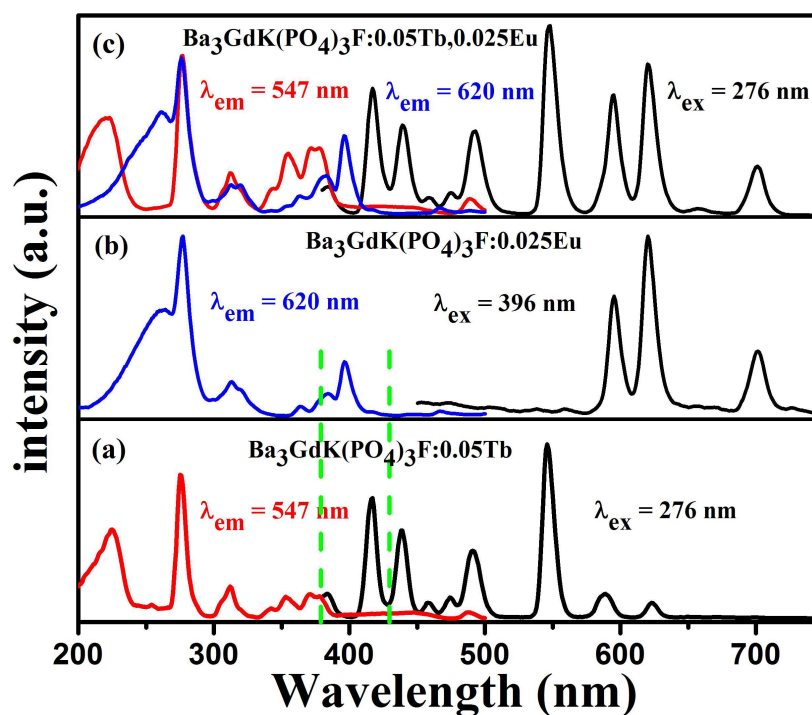

Fig. 7 The PLE and PL spectra of **(a)** the $Ba_3GdK(PO_4)_3F:0.05Tb^{3+}$ phosphor, **(b)** the $Ba_3GdK(PO_4)_3F:0.025Eu^{3+}$ phosphor, and **(c)** the $Ba_3GdK(PO_4)_3F:0.05Tb^{3+},0.025Eu^{3+}$ phosphor.

Aiming at investigating the mechanism of the energy transfer from Tb^{3+} to Eu^{3+} ions in the $Ba_3GdK(PO_4)_3F$ host, a series of samples with nominal compositions of $Ba_3Gd_{0.95-n}K(PO_4)_3F:0.05Tb^{3+},nEu^{3+}$ (n=0-0.40) were synthesized and their luminescent properties were investigate systematically. From **Fig. 8(a)** and **Fig. 8(b),**

it is found that the PL intensity of Tb^{3+} at the wavelength of 547nm become weaker with increasing the doping Eu^{3+} content. Meanwhile, the emission intensity of Eu^{3+} ions at the wavelength of 620nm increases gradually until that the concentration quenching takes place as the Eu^{3+} content reaches 0.30 mol. These results suggest an efficient energy transfer from the Tb^{3+} to Eu^{3+} ions.
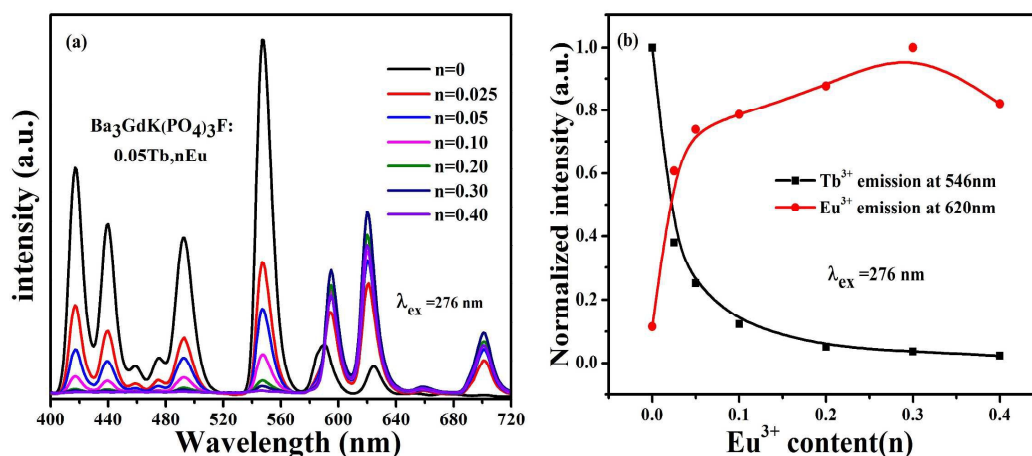

Fig. 8 (a) PL spectra of $Ba_3GdK(PO_4)_3F:0.05Tb^{3+},nEu^{3+}$ phosphors excited at 276nm. **(b)** Dependence of the normalized emission intensity of Eu^{3+} and Tb^{3+} for $Ba_3GdK(PO_4)_3F$ phosphors with varying Eu^{3+} concentration(n).

Generally, the energy-transfer efficiency (η_T) from the sensitizer to activator can be expressed by the following formula [39]:

$$\eta_T = 1 - \frac{I_x}{I_0} \qquad (1)$$

where η_T is the energy-transfer (ET) efficiency, I_0 and I_χ are the luminescence intensity of Tb^{3+} ions at 547 nm with and without Eu^{3+} ions, respectively. **Fig. 8(b)** clearly reveals the trends of gradually decreased emission intensity of Tb^{3+} ions and increased emission intensity of Eu^{3+} ions. As shown in the **Fig. 9**, one can see that the ET efficiency increases continuously with the increase of Eu^{3+} concentration.

However, the increasing rate decreases when the Eu^{3+} concentration increases. This reveals that the quantity of energy that can transfer from Tb^{3+} to Eu^{3+} is gradually restricted for high Eu^{3+} concentration owing to: (1) the concentration quenching of Eu^{3+} to a lesser extent and (2) the fixed content of Tb^{3+} ions.
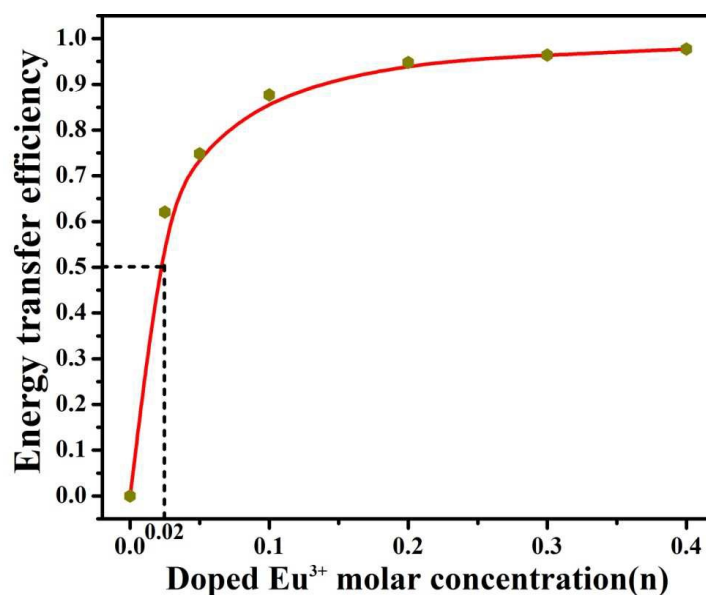

Fig. 9 Dependence of the energy-transfer efficiency η_T on the Eu^{3+} concentration (n).

Fig. 10 displays the UV−vis diffuse reflectance spectra (DRS) of $Ba_3Gd_{0.95-n}K(PO_4)_3F:0.05Tb^{3+},nEu^{3+}$ phosphors with different n values. The $Ba_3Gd_{0.95}K(PO_4)_3F:0.05Tb^{3+}$ phosphor shows energy absorption at two regions (200-240nm and 270-300nm), which are due to the f−f absorption of Tb^{3+} ions. This phenomenon is simultaneously consistent with the PLE spectra of $Ba_3Gd_{0.95}K(PO_4)_3F:0.05Tb^{3+}$ in **Fig. 7(a)**. When Eu^{3+} ions are doped into $Ba_3Gd_{0.95}K(PO_4)_3F:0.05Tb^{3+}$, the new absorption bands between 240 to 270 nm in UV region are resulted from the f-f transitions of Eu^{3+} ions. The DRS results support that $Ba_3Gd_{0.95-n}K(PO_4)_3F:0.05Tb^{3+},nEu^{3+}$ has a strong and broad absorption range, which matches well with n-UV chips as w-LEDs phosphor. Significantly, continually

decreased intensities of bands in the 200-240nm region of these phosphors were observed with increasing the Eu^{3+} concentration, which further corroborates the occurrence of energy transfer from Tb^{3+} to Eu^{3+}.
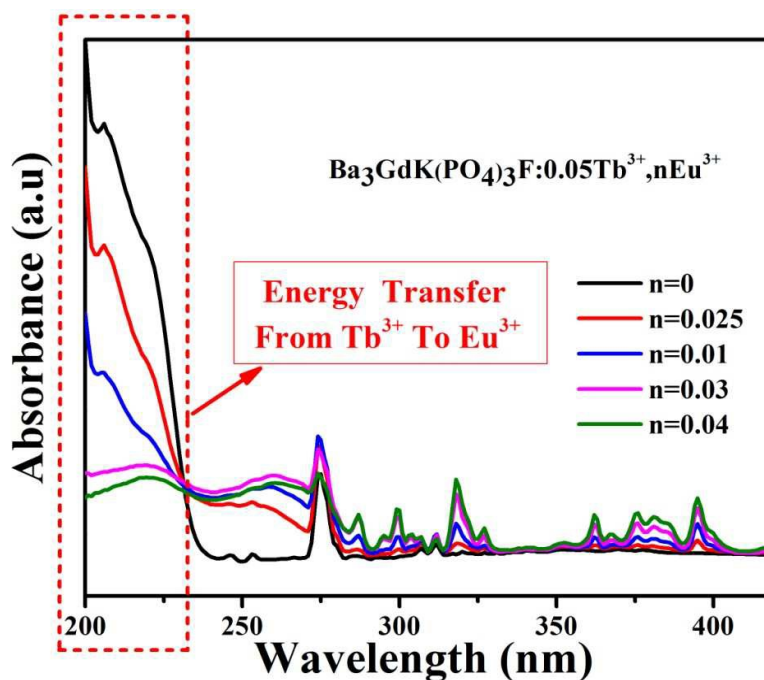

Fig. 10 UV−vis diffuse reflectance spectra for $Ba_3GdK(PO_4)_3F:0.05Tb^{3+},nEu^{3+}$.

As we know, the resonant energy-transfer mechanism from a sensitizer to an activator in a phosphor consists of two types: exchange interaction and multipolar interaction. If energy transfer takes the exchange interaction, the critical distance between sensitizer and activator should be shorter than 4Å [40]. In our $Ba_3GdK(PO_4)_3F:Tb^{3+},Eu^{3+}$ system, the critical distance R_C for energy transfer from the Tb^{3+} to Eu^{3+} ions is calculated by the concentration quenching method. The critical distance is obtained according to the following equation [41-43]:

$$R_C \approx 2\left[\frac{3V}{4\pi x_c N}\right]^{1/3} \qquad (2)$$

Here χ_c represents the critical concentration (the total concentration of Tb^{3+} and Eu^{3+}

ions at which the energy-transfer efficiency is 0.5); N is the number of cations in the unit cell and V is the volume of the unit cell. For the $Ba_3GdK(PO_4)_3F$ host, V = $629.522Å^3$, N = 6, and χ_c = 0.07, so the critical distance Rc is determined to be 14.20 Å. This value is much longer than 4 Å, proving that the energy transfer mechanism in this system is governed by the electric multipolar interaction.

On the basis of Dexter's energy-transfer expression of multipolar interaction and Reisfeld's approximation, the following relation can be obtained [44-46]:

$$\frac{\eta_o}{\eta_s} \propto C^{n/3} \qquad\qquad (3)$$

Herein, C represents the doping content of Eu^{3+}, η_0 and η_S are the luminescence quantum efficiencies of Tb^{3+} with and without the acceptor Eu^{3+}, respectively. The value of $\frac{\eta_o}{\eta_s}$ can be estimated approximately by the value of related luminescence intensity ratio ($\frac{I_{so}}{I_s}$). The n = 6, 8, and 10 correspond to the dipole-dipole, dipole-quadrupole, and quadrupole-quadrupole interactions, respectively. As shown in **Fig.11**, a linear behavior was observed only when n=6, which clearly confirms that the energy transfer from the Tb^{3+} to Eu^{3+} ions occurs via dipole-dipole mechanism.
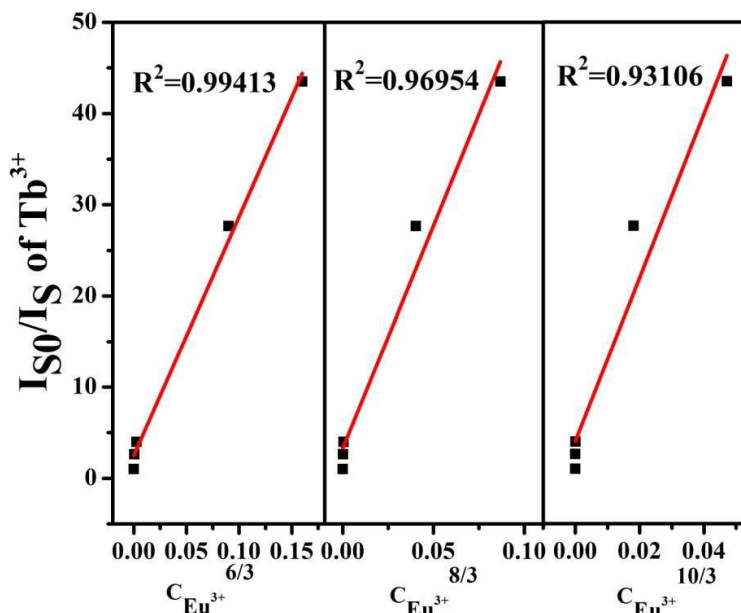
Fig.11 Dependence of I_{S0}/I_S of Tb^{3+} on (a) $C_{Eu3+}^{6/3}$, (b) $C_{Eu3+}^{8/3}$ and (c) $C_{Eu3+}^{10/3}$.

Fig. 12 illustrates the proposed diagram of energy transfer between $Tb^{3+} \rightarrow Eu^{3+}$ in the $Ba_3GdK(PO_4)_3F:Tb^{3+},Eu^{3+}$ phosphors. Upon VUV−UV excitation, excited electrons shift to the $^5D_4$ or $^5D_3$ excited state of Tb^{3+} after multistep relaxations. Then the electrons of the Tb^{3+} ions shift from the $^5D_4$ or $^5D_3$ excited state to the ^7F_J ground state, resulting in generation of green or blue light. Meanwhile, the excited electrons of the Tb^{3+} ions may move to the $^5D_1$ excited state of Eu^{3+} ions by the energy transfer from Tb^{3+} to Eu^{3+} ions. Finally, red light gives out due to the electrons relax to $^5D_0$ state and $^5D_0 \rightarrow {}^7F_J$ (J = 1, 2, 3, 4) transitions of Eu^{3+} ions.
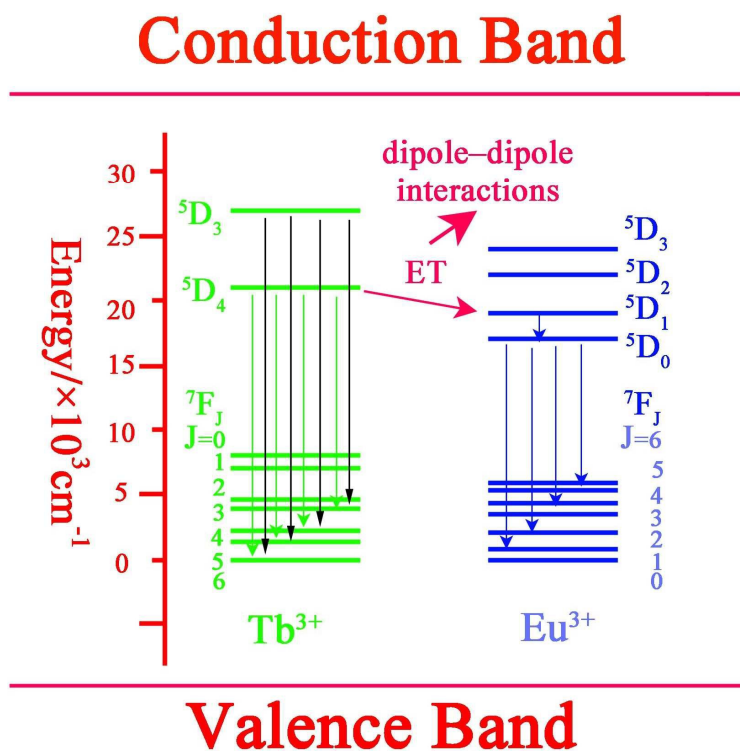
Fig. 12 Schematic energy level diagram displaying the energy transfer among Tb^{3+} and Eu^{3+} in $Ba_3GdK(PO_4)_3F$: Tb^{3+}, Eu^{3+} phosphor.

In order to investigate the luminescence dynamics, we measured the PL decay curves of $Ba_3Gd_{0.95-n}K(PO_4)_3F$:$0.05Tb^{3+}$,$nEu^{3+}$ excited at 368 nm and monitored at 547 nm, and then calculated the lifetime. From **Fig. 13**, we can see that the decay curves of the Tb^{3+} emission deviate slightly from a single exponential rule ($I = I_0 \exp(-t/t)$) [47] at lower Eu^{3+} concentration and the deviations become more obvious with the increase of Eu^{3+} content. The effective lifetime of the decay curves for Tb^{3+} emission can be determined using the following equation [48-49]:

$$\tau = \frac{\int_0^\infty I(t)\,t\,dt}{\int_0^\infty I(t)\,dt} \tag{4}$$

Where I(t) is the intensity at time t. From equation (4), the effective lifetime were

determined to be 1.19, 0.945, 0.717, and 0.629 ms for $Ba_3Gd_{0.95-n}K(PO_4)_3F$:

$0.05Tb^{3+},nEu^{3+}$ samples with n = 0, 0.05, 0.20, and 0.40, respectively. The decay time

decreases monotonically with an increase in the Eu^{3+} doping content, which strongly

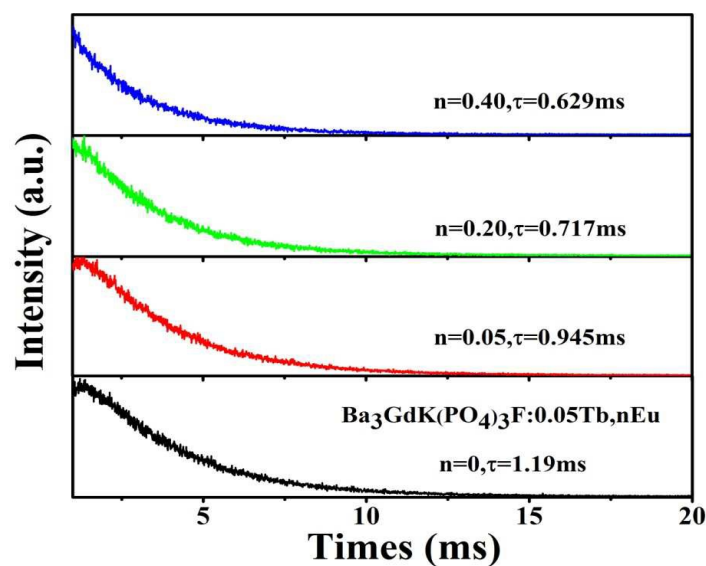demonstrates the energy transfer from Tb^{3+} to Eu^{3+}.

Fig. 13 Photoluminescence decay curves and lifetime of Tb^{3+} in $Ba_3GdK(PO_4)_3F$: $0.05Tb^{3+},nEu^{3+}$

(excited at 368 nm, monitored at 543 nm).

With regard to high power LED applications, thermal stability is a technologically

important consideration for LED phosphors. In order to investigate the influence of

temperature on luminescence, the temperature-dependent PL spectra for

$Ba_3Gd_{0.95}K(PO_4)_3F:0.05Tb^{3+}$ and $Ba_3Gd_{0.925}K(PO_4)_3F:0.05Tb^{3+},0.025Eu^{3+}$ under

excitation at 276 nm are portrayed in **Fig. 14**. As displayed in **Fig. 14(a)**, the emission

intensity of $Ba_3Gd_{0.95}K(PO_4)_3F:0.05Tb^{3+}$ only slightly changes as the temperature

varies from 25 to 300 ℃ , indicating the excellent thermal stability of

$Ba_3Gd_{0.95}K(PO_4)_3F:0.05Tb^{3+}$ sample. From **Fig. 14(b)** and **Fig. 14(c),** we can see that

the PL intensity decreases slowly with increasing the temperature. At 150℃, the

normalized   PL   intensity   of   the Tb^{3+} and Eu^{3+} ions   in

$Ba_3Gd_{0.975}K(PO_4)_3F:0.05Tb^{3+},0.025Eu^{3+}$ decreased by 53.8% and 85.8% of the initial

value at 25 $^{\circ}$C, respectively. To better understand the temperature dependence of

photoluminescence, activation energy (E), as an important parameter, is calculated.

The activation energy for thermal quenching is estimated using the Arrhenius

equation [50-52]:

$$I(T) \approx \frac{I_0}{1+c\exp(\frac{-E}{kT})} \qquad\qquad (5)$$

Where I_0 and I (T) represent the initial luminescence intensit and the intensity at

temperature T, respectively. C is a constant, E is the activation energy for thermal

quenching, and k is Boltzmann's constant (8.629×10^{-5} eV/K). The plot of $\ln[(I_0/I)-1]$

against 1/(kT) for $Ba_3GdK(PO_4)_3F:0.05Tb^{3+},0.025Eu^{3+}$ is demonstrated in **Fig.14(d)**.

The values of activation energy E are calculated to be 0.253eV and 0.137eV for the

peak intensities of the $^5D_0$ to$^7F_2$ transition of Eu^{3+} and $^5D_4–^7F_5$ transition of Tb^{3+} in

$Ba_3GdK(PO_4)_3F:0.05Tb^{3+},0.025Eu^{3+}$ phosphor, respectively. It can be concluded that

the relatively high activation energy E resulting in the excellent thermal stability of
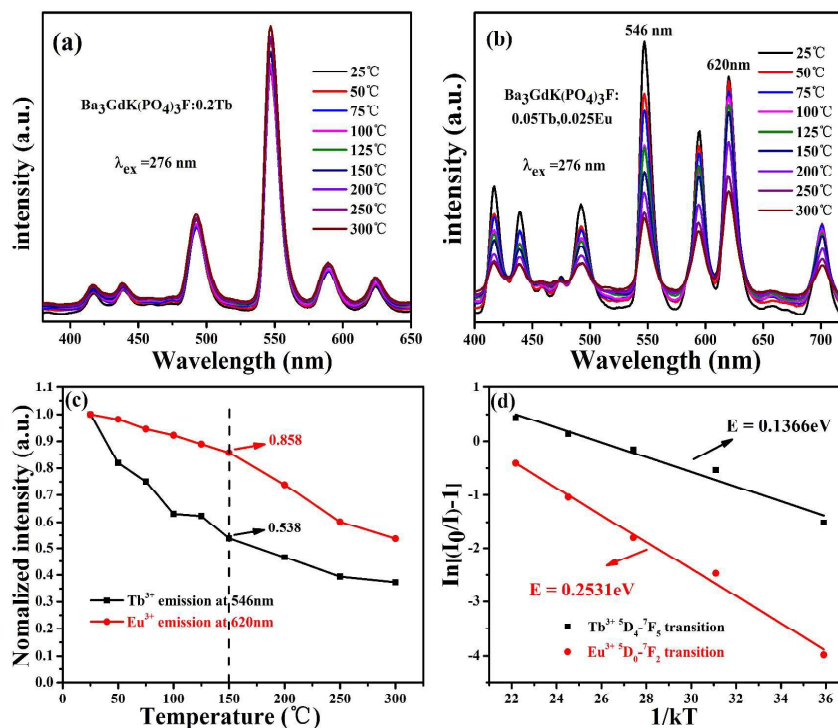
our phosphors.

Fig14. PL spectra (λ_{ex} = 276 nm) of $Ba_3GdK(PO_4)_3F:0.2Tb^{3+}$ **(a)**, and $Ba_3GdK(PO_4)_3F$: $0.05Tb^{3+},0.025Eu^{3+}$ **(b)** Phosphors under different temperatures in the range of 25–300 ℃. Integrated intensity of both Tb^{3+} and Eu^{3+} ions is given in **(c)**. The activation energy graph for thermal quenching is shown in **(d)**.

The Commission Internationale de L'Eclairage (CIE) chromaticity coordinates, correlated color temperature (CCT), and quantum efficiency (QY) for the $Ba_3Gd_{0.95-n}K(PO_4)_3F:0.05Tb^{3+},nEu^{3+}$ (n=0-0.40) phosphors are summarized in **Table 2**. **Fig.15** depicts the CIE chromaticity coordinates of the $Ba_3Gd_{0.95-n}K(PO_4)_3F:0.05Tb^{3+},nEu^{3+}$ phosphors at excitation wavelength of 276nm and the digital photos of the phosphors under 365nm UV lamp excitation. With increasing the Eu^{3+}content from 0 to 0.40, the coordinates shift from blue-greenish (0.238, 0.311) to orange (0.521, 0.335). In particular, a warm white light (0.31, 0.33) was realized in $Ba_3Gd_{0.925}K(PO_4)_3F:0.05Tb^{3+},0.025Eu^{3+}$. Meanwhile, it is found from **Table 2** that the color temperature of the samples was modulated from 12860 to

1753K with increasing the value of n. The CCT of the white light emitting phosphor $Ba_3Gd_{0.925}K(PO_4)_3F:0.05Tb^{3+},0.025Eu^{3+}$ is 5068K, confirming that this light is warm-white-light. As shown in **Table 2**, the QY values for $Ba_3Gd_{0.95-n}K(PO_4)_3F:0.05Tb^{3+},nEu^{3+}$ decline with elevating the n value. The Color rendering index (CRI) values for $Ba_3Gd_{0.95-n}K(PO_4)_3F:0.05Tb^{3+},nEu^{3+}$($n$ =0，0.025) phosphors excited at 276 nm are plotted in **Table 3**. It can be observed that the CRI value and CCT of $Ba_3Gd_{0.95-n}K(PO_4)_3F:0.05Tb^{3+},0.025Eu^{3+}$ phosphor are 84 and 5068K, confirming that this phosphor be used as a potential warm-white-emitting phosphor for white-light NUV LEDs.
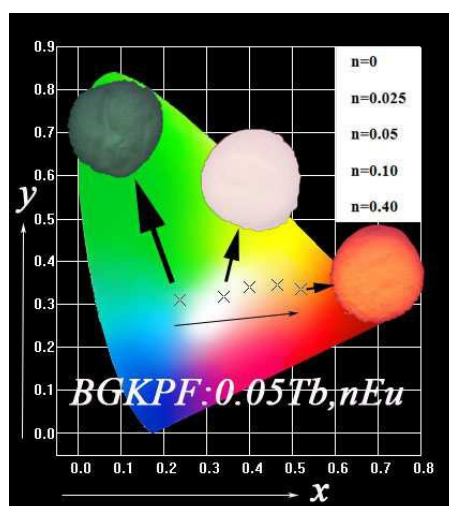

Fig. 15 CIE chromaticity diagram of BGKPF($Ba_3Gd_{0.95-n}K(PO_4)_3F$):0.05Tb^{3+},nEu^{3+} phosphors excited at 276nm, and the digital photos of the samples under 365 nm UV lamp excitation.

Table2. Comparison of the CIE chromaticity coordinates (x, y), CCT, and QE values for $Ba_3Gd_{1-0.05-n}K(PO_4)_3F: 0.05Tb^{3+},nEu^{3+}$ phosphors under excitation at 276 nm.

Sample No.	Sample composition (n)	CIE coordinates (x, y)	CCT (K)	QE values (%)
1	0	(0.238, 0.311)	12860	19.3
2	0.025	(0.341, 0.318)	5068	10.4

3	0.05	(0.401, 0.339)	3131	6.45
4	0.10	(0.465, 0.345)	2069	5.18
5	0.20	(0.511, 0.341)	1758	4.32
6	0.30	(0.529, 0.339)	1758	3.29
7	0.40	(0.521, 0.335)	1753	2.17

Table3. Color rendering index (CRI) for $Ba_3Gd_{0.95-n}K(PO_4)_3F:0.05Tb^{3+},nEu^{3+}(n =0, 0.025)$ phosphors excited at 276 nm.

Sample composition (n)	n=0	n=0.025
CRI	41	84

4. Conclusion

In conclusion, we have prepared a series of color-tunable apatite-structured $Ba_3Gd_{1-m-n}K(PO_4)_3F: mTb^{3+},nEu^{3+}$ phosphors by high-temperature solid-state reaction for the first time. The powder X-ray diffraction patterns and Rietveld refinement demonstrate that the $Ba_3GdK(PO_4)_3F$ host has an hexagonal crystal structure with cell parameters $a = b = 9.855(36)$ Å, $c = 7.484(02)$ Å, and $V = 629.522$Å^3. The luminescence properties and energy-transfer behavior of the as-prepared samples have been investigated in detail. The spectral overlap between the PL of Tb^{3+} and the PLE of Eu^{3+} indicated the existence of energy transfer between Tb^{3+} and Eu^{3+} occurs. The energy transfer critical distance between Tb^{3+} and Eu^{3+} was calculated to be 14.20 Å by the concentration quenching method, and the resonant energy-transfer mechanism is determined to be dipole-dipole interaction. The energy transfer efficiency increases with enhancing Eu^{3+} concentration, and the η_T value was calculated to be 0.977 when the content of Eu^{3+} was up to 0.40 mol. More importantly, a superior warm white light

emission of $Ba_3Gd_{0.925}K(PO_4)_3F:0.05Tb^{3+},0.025Eu^{3+}$ with CIE coordinates of (0.341, 0.318) and a CCT of 5068K was realized. Temperature-dependent PL spectra reveal that the normalized PL intensity of the Tb^{3+} and Eu^{3+} ions in $Ba_3Gd_{0.925}K(PO_4)_3F:0.05Tb^{3+},0.025Eu^{3+}$ can still remain 53.8% and 85.8% of the initial intensity even though the temperature increase up to 150°C. In addition, based on the Arrhenius equation, the activation energies for thermal quenching of $Ba_3Gd_{0.925}K(PO_4)_3F: 0.05Tb^{3+}, 0.025Eu^{3+}$ are estimated to be 0.253eV and 0.137eV for the intensity of the $^5D_0$ to$^7F_2$ transition of Eu^{3+} and $^5D_4 - {}^7F_5$ transition of Tb^{3+} in $Ba_3Gd_{0.925}K(PO_4)_3F:0.05Tb^{3+}, 0.025Eu^{3+}$ phosphor, respectively.

References

1 Wen, D. W.; Shi, J. X.; Wu, M. M.; Su, Q. *ACS Appl. Mater. Interfaces* 2014, **6**, 10792.

2 Xu, J.; Shi, Y.; Xie, J. J.; Lei, F. *J. Am. Ceram. Soc.,* 2013, **96 [6]**, 1930.

3 Li, K.; Shang, M. M.; Geng, D. L.; Lian, H. Z.; Zhang, Y.; Fan, J.; Lin, J. *Inorg. Chem.* 2014, **53**, 6743.

4 Yeh, C. W.; Chen, W. T.; Liu, R. S.; Hu, S. F.; Sheu, H. S.; Chen, J. M.; Hintzen, H. T. *J. Am. Chem. Soc.* 2012, **134**, 14108.

5 Bachmann, V.; Ronda, C.; Meijerink, A. *Chem. Mater*. 2009**, 21**, 2077.

6 Huang, C. H.; Chen, T. M. *Inorg. Chem.* 2011, **50**, 5725.

7 Huang, W. Y.; Yoshimura, F.; Ueda, K.; Shimomura, Y.; Sheu, H. S.; Chan, T. S.; Chiang, C. Y.; Zhou, W. Z.; Liu, R. S. *Chem. Mater.,* 2014, **26 (6)**, pp 2075.

8 Xia, Z.G.; Zhang, Y. Y.; Molokeev, M. S.; Atuchin, V.V. *J. Phys. Chem. C* 2013, **117**, 20847.

9 Brgoch, J.; Borg, C. K. H.; Denault, K. A.; Mikhailovsky, A.; DenBaars, S. P.; Seshadri, R. *Inorg. Chem.* 2013*,* **52***,* 8010.

10 Hecht, C.; Stadler, F.; Schmidt, P. J.; Gu¨nne, J. S. A. D.; Baumann, V.; Schnick, W. *Chem. Mater.* 2009, **21**, 1595.

11 Chen, J.; Liu, Y. G.; Fang, M. H.; Huang, Z. H. *Inorg. Chem.*, 2014, **53** *(21)*, pp 11396.

12 Huang, C. H.; Chiu, Y. C.; Yeh, Y. T.; Chan, T. S.; Chen, T. M. *ACS Appl. Mater. Interfaces* 2012*,* **4***,* 6661.

13 Hou, J. S.; Jiang, W. Z.; Fang, Y. Z.; Huang, F. Q. *J. Mater. Chem. C,* 2013*,* 1,*5892.

14 Jia, Y. C.; Lu¨, W.; Guo, N.; Lu¨, W. Z.; Zhao, Q.; You, H. P. *Phys.Chem. Chem. Phys.,* 2013*,* **15***,* 13810.

15 Zhang, C. H.; Liang, H.; B.; Zhang, S.; Liu, C. M.; Hou, D. J.; Zhou, L.; Zhang, G. B.; Shi, J. Y. *J. Phys. Chem. C* 2012*,* **116***,* 15932.

16 Jiao, M. M.; Guo, N.; Lü, W.; Jia, Y.C.; Lv,W. Z.; Zhao, Q.; Shao, B.Q.; You, H. P. *Dalton Trans.,* 2013, **42**, 12395.

17 Gu, J. L.; Zhong, J. P.; Liang, H. B.; Zhang, J. H.; Su, Q. *Chemical Physics Letters* 2014, **592**, 261.

18 Liang, Z.J.; Mo, F. W.; Zhang, X. G.; Zhoun, L. Y.; Chen, P. C.; Xu, C. Y. *Ceramics International* 2014*,* **40***,* 7501.

19 Ingle, J. T.; Gawande, A. B.; Sonekar, R. P.; Omanwar, S. K.; Wangd, Y. H.; Zhao, L. *Journal of Alloys and Compounds* 2014*,* **585**, 633.

20 Zhang, X. G.; Zhou, L. Y.; Shi, J. X.; Gong, M .L. *Materials Letters* 2014, **137**, 32.

21 Jiao, M. M.; Guo, N.; Lü, W.; Jia, Y. C.; Lv, W. Z.; Zhao, Q.; Shao, B. Q.; You, H. P. *Inorg. Chem.,* 2013, 52 (18), pp 10340.

22 Wen, Y.; Wang, Y.; Zhang, F.; Liu, B. *Mater. Chem. Phys.* 2011, **129**, 1171.

23 Li, K.; Geng, D. L.; Shang, M. M.; Zhang, Y.; Lian, H. Z.; Lin, J. *J. Phys. Chem. C* 2014, **118**, 11026.

24 Zhou, L.; Liang, H. B.; Tanner, P. A.; Zhang, S.; Hou, D. J.; Liu, C. M.; Tao, Y.; Huang, Y.; Li, L. N. *J. Mater. Chem.* C, 2013, **1**, 7155.

25 Guo, N.; You, H. P.; Jia, C. Z.; Ouyang, R.; Wu, D. H. *Dalton Trans.,* 2014, 43, 12373.

26 Hu, S. S.; Tang, W. J. *Journal of Luminescence* 2014, **145**, 100.

27 Larson, C.; Von Dreele, R. B. *Los Alamos, NM,* 1994, 86.

28 Mathew, M.; Mayer, I.; Dickens, B.; Schroeder, L. W. *Journal of Solid State Chemistry.* 1979, **28**, 79.

29 Shannon, R. D. *Acta Crystallographic a.* 1976. **A32**, 751.

30 Van Uitert, L. G. *J. Electrochem. Soc.* 1967, **114**, 1048.

31 Xia, Z. G.; Zhuang, J. Q.; Liao, L. B. *Inorg. Chem.* 2012, **51**, 7202.

32 Chen, Y. Q.; Yang, H. K.; Park, S. W.; Moon, B. K.; Choi, B. C.; Jeong, J. H.; Kim, K. H. *Journal of Alloys and Compounds* 2012, **511**, 123.

33 Geng, D. L.; Shang, M. M.; Zhang, Y.; Lian, H. Z.; Lin, J. *Inorg.*

Chem., 2013, **52 (23)**, pp 13708.

34 Yang, J.; Zhang, C. M.; Li, C. X.; Yu, Y. N.; Lin, J. *Inorg. Chem.* 2008, **47**, 7262.

35 Jia, Y. C.; Lu¨, W.; Guo, N.; Lu¨, W. Z.; Zhao, Q.; You, H. P. *Phys. Chem. Chem. Phys.,* 2013, **15**, 60572.

36 Zhang, X. M.; Wang, J.; Guo, K.; Chen, H. H.; Yang, X. X.; Zhao, J. T.; *Journal of Alloys and Compounds* 2012, **517**, 149– 156.

37 Rambabu, U.; Han, S. D. *RSC Advances,* 2013, **3**, 1368.

38 Liu, C. M.; Hou, D. J.; Yan, J.; Zhou, L.; Kuang, X. J.; Liang, H. B.; Huang, Y.; Zhang, B. B.; Tao, Y. *J. Phys. Chem. C* 2014, **118**, 3220.

39 Dai, W. B. *RSC ADV.,* 2013, **10**, 1.

40 Zhang, Y. Y.; Xia, Z. G.; Liu, H. K.; Wang, Z. Y.; Li, M. L. *Chemical Physics Letters* 2014, **593**, 189.

41 Liu, H. K.; Liao L. B.; Xia, Z. G. *RSC Adv.,* 2014, **4**, 7288.

42 Li, H. F.; Zhao, R.; Jia, Y. L.; Sun, W. Z.; Fu, J. P.; Jiang, L. H.; Zhang, S.; Pang, R.; Li, C. Y. *ACS APPLIED MATERIALS & INTERFACES,* 2014, **6 (5)**, 3163.

43 Im, W. B.; Brinkley, S.; Hu, J.; Mikhailovsky, A.; DenBaars, S. P.; Seshadri, R. *Chem. Mater.* 2010, **22**, 2842.

44 Liu, H. K.; Luo, Y.; Mao, Z. Y.; Liao, L. B.; Xia, Z. G. *J. Mater. Chem. C,* 2014, **2**, 1619.

45 Yang, W. J.; Luo, L. Y.; Chen, T. M.; and Wang, N. S. *Chem. Mater.* 2005, **17,** 3883.

46 Huang, C. H.; Kuo, T. W.; Chen, T. M. *ACS Appl Mater Interfaces* 2010 May;

2(5): 1395.

47 Li, G. G.; Zhang, Y.; Geng, D. L.; Shang, M. M.; Peng, C.; Cheng, Z. Y.; Lin, J. *ACS Appl. Mater. Interfaces* 2012, **4**, 296.

48 Guo, N.; Zheng, Y. H.; Jia, Y. C.; Qiao, H.; You, H. P. *New. J. Chem.,* 2012*,* **36**, 168.

49 Xia, Z. G.; Liu, R. S. *J. Phys. Chem. C* 2012, 116, 15604.

50 Zhang, X. G.; Zhou, L. Y.; Pang, Q.; Shi, J. X.; Gong, M. L. *J. Phys. Chem. C* 2014, **118**, 7591.

51 Luo, Y.; Xia, Z. G. *J. Phys. Chem. C* 2014, **118**, 23297.

52 Zhang, S. Y.; Nakai, Y.; Tsuboi, T.; Huang, Y. L.; Seo, H. J. *Chem. Mater.* 2011, **23**, 1216.